

Article

# A $\pi$ - $\pi$ Stacked High-Performance Organic Anode for Durable Rocking-Chair Zinc-Ion Battery

Yuyan Tang <sup>1</sup>, Shaohui Li <sup>1</sup>, Meng-Fang Lin <sup>2</sup>, Jingwei Chen <sup>3,\*</sup>, Alice Lee-Sie Eh <sup>4,\*</sup> and Qun Xu <sup>1,5,\*</sup>

<sup>1</sup> School of Materials Science and Engineering, Zhengzhou University, Zhengzhou 450001, China; shaohuili@zzu.edu.cn (S.L.)

<sup>2</sup> Department of Materials Engineering, Ming Chi University of Technology, New Taipei City 24301, Taiwan

<sup>3</sup> School of Materials Science and Engineering, Ocean University of China, Qingdao 266100, China

<sup>4</sup> Metrohm Singapore Pte Ltd., 31 Toh Guan Road East, #06-08 LW Techno Centre, Singapore 608608, Singapore

<sup>5</sup> Henan Institute of Advanced Technology, Zhengzhou University, Zhengzhou 450001, China

\* Correspondence: chenjingwei@ouc.edu.cn (J.C.); alice.eh@metrohm.com.sg (A.L.-S.E.); qunxu@zzu.edu.cn (Q.X.)

**Abstract:** Sustainable organic materials have gained considerable attention as electrodes for zinc-ion batteries (ZIB) due to their high theoretical capacity, structural versatility, and environmental friendliness. However, issues of inferior capacities and poor rate performance owing to limited inherent electronic conductivity and severe dissolution still persist. Herein, sandwich-structured perylene diimide-ethylene diamine/graphene (PDI-EDA/EG) composites are judiciously designed and synthesized. The two-dimensional graphene host can interact with the PDI-EDA polymer through  $\pi$ - $\pi$  stacking, endowing accelerated ion/electron transfer, abundant active sites, excellent structural integrity, and mitigated solubility of the hybrid electrodes. When evaluated as an anode in ZIB, the hybrid electrode delivers a high capacity ( $110.2 \text{ mAh g}^{-1}$  at  $0.1 \text{ A g}^{-1}$ ), superior rate capability ( $88.9 \text{ mAh g}^{-1}$  at  $5 \text{ A g}^{-1}$ ), and exceptional durability (93.4% capacity retained after 1000 cycles). The structure evolution of the hybrid electrode during the insertion/extraction cycle was investigated by ex-situ Fourier transform infrared spectra (FTIR) and X-ray photoelectron spectroscopy (XPS), revealing the reversible  $\text{Zn}^{2+}$  storage at carbonyl sites. In addition, a prototype rocking-chair ZIB cell was constructed with a zinc pre-intercalated  $\text{MnO}_2$  cathode, displaying an ultrahigh energy density of  $54.9 \text{ Wh kg}^{-1}$  at a power density of  $42.5 \text{ W kg}^{-1}$  and excellent stability with negligible capacity decay after 1000 cycles.

**Keywords:** zinc-ion battery; rocking-chair battery; organic anode; aqueous electrolyte; perylene diimide-ethylene diamine



**Citation:** Tang, Y.; Li, S.; Lin, M.-F.; Chen, J.; Eh, A.L.-S.; Xu, Q. A  $\pi$ - $\pi$  Stacked High-Performance Organic Anode for Durable Rocking-Chair Zinc-Ion Battery. *Batteries* **2023**, *9*, 318. <https://doi.org/10.3390/batteries9060318>

Academic Editor: Hirotoshi Yamada

Received: 15 April 2023

Revised: 29 May 2023

Accepted: 5 June 2023

Published: 8 June 2023



**Copyright:** © 2023 by the authors. Licensee MDPI, Basel, Switzerland. This article is an open access article distributed under the terms and conditions of the Creative Commons Attribution (CC BY) license (<https://creativecommons.org/licenses/by/4.0/>).

## 1. Introduction

Rechargeable aqueous zinc-ion batteries (ZIBs) have attracted considerable interest and show great promise for grid-level energy storage owing to their moderate energy density, environmental friendliness, abundant reserves, cost-effectiveness, inherent reliability, and high ion conductivity of the electrolytes [1–5]. Over the past few years, great achievements have been made in developing advanced cathode materials, including Mn-, V-, and Co-based compounds, Prussian blue analogues, organic compounds, and metal-organic frameworks (MOFs) [6–10]. However, in most full-cell prototypes, excessive Zn metal (Zn foil, Zn powder, etc.) was applied as an anode based on the reversible  $\text{Zn}^{2+}$  plating/stripping due to the high theoretical gravimetric capacity ( $820 \text{ mAh g}^{-1}$ ), suitable redox potential ( $-0.76 \text{ V}$  vs. standard hydrogen electrode), low cost, and good stability in the ambient environment of Zn [4,11–13]. Unfortunately, zinc metal anodes suffer from various drawbacks, such as uncontrollable zinc dendrites growth, corrosive reaction, hydrogen evolution reaction (HER), and low Coulombic efficiency, sacrificing rate

performance and lifespan [14–16]. Although tremendous efforts such as surface modification, structural design, hydrogel electrolyte adoption, and multi-functional separator construction have been made to restrict the growth of zinc dendrites, issues of limited stability still pertain to zinc metal anodes [15–22].

As the dominant energy storage device in the market, the successful commercialization of lithium-ion batteries (LIBs) is attributed to the introduction of an intercalation-type graphite anode instead of lithium, which can effectively inhibit the problems caused by lithium dendrites. Thus, inspired by the achievements and experience of LIBs, it is of great value to construct zinc-free “rocking-chair” ZIBs, which can overcome the limitations of Zn anodes. An ideal anode material should possess a high theoretical capacity, robust structural stability, reversible  $\text{Zn}^{2+}$  insertion/extraction and low potential vs.  $\text{Zn}/\text{Zn}^{2+}$  [19–25]. In 2016, Chevrel-phase  $\text{Mo}_6\text{S}_8$  was investigated as a ZIBs anode and demonstrated a low average discharge plateau of 0.36 V vs.  $\text{Zn}/\text{Zn}^{2+}$  with good cycling stability yet an insatiable capacity [26]. In the meantime, Manthiram et al. found that the  $\text{Zn}^{2+}$  pre-intercalated binary molybdenum-vanadium oxide ( $\text{Zn}_x\text{Mo}_{2.5+y}\text{VO}_{9+z}$ ) can also be applied as an anode to store the  $\text{Zn}^{2+}$  [27]. Since then, numerous ZIB anodes have been discovered, such as  $\text{Cu}_{2-x}\text{Se}$ ,  $\text{WO}_3/\text{WC}$ ,  $\text{CuS}_{1-x}\text{@PANI}$ ,  $\text{h-MoO}_3$ ,  $\text{Cu}_7\text{Te}_4$ , and hydrated ammonium vanadate [20–22,28–32]. These inorganic anodes mainly rely on the insertion and conversion-based electrochemical mechanisms, which are thus accompanied by sluggish diffusion kinetics and rapid fading of capacity.

Compared to inorganic anodes, organic compounds, particularly carbonyl-rich molecules and polymers, are considered favorable anode candidates due to their tunable chemical structure, environmental friendliness, and recyclability [7–9,33–35]. In addition, the redox processes of organic compounds mainly relied on chem-absorption and chemical bond rearrangement without structure or valence variations, thus manifesting fast  $\text{Zn}^{2+}$  adsorption/desorption with structural integrity [8]. For example, Lu et al. reported the 3, 4, 9, 10-perylenetetracarboxylic dianhydride anode for  $\text{Zn}^{2+}$  storage, which exhibits a remarkable capacity of  $122.9 \text{ mAh g}^{-1}$  owing to the 1-D ion tunnels and strengthened  $\pi$ - $\pi$  stacking interaction [36]. Zhang et al. constructed a perylene-3, -4, -9, -10-tetracarboxylic diimide/reduced graphene oxide (PTCDI/rGO) composite electrode, which demonstrated a high capacity of  $121 \text{ mAh g}^{-1}$  through the  $\text{H}^+$ - $\text{Zn}^{2+}$  co-participating phase transfer mechanism [37]. However, it remains a major difficulty to obtain high capacity, remarkable rate capability, and excellent stability in organic anodes for ZIBs due to their dissolution in electrolytes, intrinsically poor electronic conductivity, and relatively high discharge plateau.

In this study, a sandwich-structured perylene diimide-ethylene diamine/graphene (PDI-EDA/EG) composite electrode was designed with effectively boosted  $\text{Zn}^{2+}$  storage capacity and electrochemical kinetics. Owing to the strong  $\pi$ - $\pi$  stacking interactions between graphene and PDI-EDA and the high electronic conductivity of electrochemically exfoliated graphene, the electrode with unique architecture manifests greatly improved structural integrity and promotes ion/electron transport. The obtained composites exhibit a high capacity of  $110.2 \text{ mAh g}^{-1}$  at  $0.1 \text{ A g}^{-1}$  and a high rate capacity of  $88.9 \text{ mAh g}^{-1}$  at  $5 \text{ A g}^{-1}$ . The  $\text{Zn}^{2+}$  storage mechanism of PDI-EDA/EG was investigated by ex-situ Fourier transform infrared spectra (FTIR) and X-ray photoelectron spectroscopy (XPS), revealing reversible  $\text{Zn}^{2+}$  storage at carbonyl sites. To evaluate its practical application, the PDI-EDA/EG anode was combined with a  $\text{Zn}_x\text{MnO}_2$  cathode, assembling a rocking-chair ZIB with a high energy density ( $54.9 \text{ Wh kg}^{-1}$  at a power of  $42.5 \text{ W kg}^{-1}$ ) and outstanding cycle stability (without capacity degradation after 1000 cycles).

## 2. Materials and Methods

### 2.1. Materials

3, 4, 9, 10-perylenetetracarboxylic dianhydride (PTCDA, 99%), ethylene diamine (EDA, 99.5%), *N,N*-dimethylformamide (DMF, 99.8%), *N*-Methyl pyrrolidone (NMP), polyvinylidene fluoride (PVDF, 99.8%), and zinc foil (Zn, 99%) were purchased from Shang-

hai Aladdin Biochemical Technology Co., Ltd (Shanghai, China). Ammonium sulfate ( $(\text{NH}_4)_2\text{SO}_4$ , 99%), zinc sulfate heptahydrate ( $\text{ZnSO}_4 \cdot 7\text{H}_2\text{O}$ , 99.5%), manganese sulfide tetrahydrate ( $\text{MnSO}_4 \cdot 4\text{H}_2\text{O}$ ), and graphite paper were purchased from Shanghai Macklin Biochemical Co., Ltd (Shanghai, China). All the materials were used directly without any further purification.

## 2.2. Synthesis of Materials

Preparation of exfoliated graphene nanosheets (EG): The exfoliated graphene nanosheets were prepared by electrochemically exfoliating graphite paper, as previously reported [38]. Then, the stable graphene suspension dispersed in DMF was diluted to  $2 \text{ mg mL}^{-1}$  for further use.

Preparation of PDI-EDA/EG: Typically, 53.3 mg ethylene diamine (EDA) and 346.8 mg 3, 4, 9, 10-perylenetracarboxylic dianhydride (PTCDA) were added to 50 mL of EG solution ( $2 \text{ mg mL}^{-1}$ ). The resultant mixture was stirred magnetically for 3 h. To optimize the content of EG in the composites, the mass ratios of EG in the composites were controlled to 10, 20, and 30%, respectively. The resulting suspension was then poured into a 100 mL autoclave reactor for solvothermal reaction at  $180^\circ\text{C}$  for 12 h. After the reactor was cooled down, the composite was separated by centrifugation, rinsing, and drying. In the controlled experiment, pure PDI-EDA was prepared using the same synthetic procedure in the absence of EG.

## 2.3. Characterization

The crystal structure of the composites was analyzed by powder X-ray diffraction (XRD, X'Pert Pro MPD, Panalytical, Almelo, The Netherlands) using a  $\text{Cu K}\alpha$  X-ray source. The chemical structure of the composites was studied by Fourier transform infrared spectroscopy (FTIR, Thermo Scientific Nicolet, Thermo Fisher, Waltham, MA, USA) using a KBr pallet and Raman spectroscopy (Horiba LabRAM HR Evolution, Horiba Scientific, Kyoto, Japan). The micro- and nano-structures were characterized by field-emission scanning electron microscopes (FESEM, ZEISS GeminiSEM 300, ZEISS, Oberkochen, Germany). The chemical bonding environment of elements was examined on an X-ray photoelectron spectroscopy system (XPS, Thermo Scientific K-Alpha, Thermo Fisher, USA).

## 2.4. Electrochemical Measurements

All the electrochemical experiments were performed on CR2032-type coin cells. The PDI-EDA/EG electrodes were prepared by mechanically mixing active materials, carbon black (CB), and PVDF binder in a mass ratio of 7:2:1 in NMP. The slurries were drop coated onto carbon paper and dried at  $80^\circ\text{C}$  for 12 h to remove the organic solvent. The active material loading was approximately  $1\text{--}1.5 \text{ mg cm}^{-2}$ . To evaluate the electrochemical performance of organic electrodes, zinc foil, glass fiber membrane (whatman, GF/D, Austin, TX, USA), and 2 M  $\text{ZnSO}_4$  were used as counter/reference electrodes, separators, and electrolytes, respectively. The cyclic voltammetry (CV) and electrochemical impedance spectra (EIS) were measured on an electrochemical workstation (SP-150, Biologic, Seyssinet-Pariset, France). Galvanostatic charge-discharge (GCD) tests were carried out on a Neware battery test system (CT-4008) in the potential range of 0.15 to 1.2 V (vs.  $\text{Zn}/\text{Zn}^{2+}$ ). Galvanostatic intermittent titration technique (GITT) tests were performed by discharging 300 s at  $50 \text{ mA g}^{-1}$ , followed by 300 s relaxation.

For the preparation of rocking-chair type zinc-ion batteries, the PDI-EDA/EG-20,  $\text{Zn}_x\text{MnO}_2$ , glass fiber filter, and 2 M  $\text{ZnSO}_4$  + 0.1 M  $\text{MnSO}_4$  aqueous solution were used as the anode, cathode, separator, and electrolyte, respectively. The N/P mass ratio is kept at about 1.2.  $\text{Zn}_x\text{MnO}_2$  cathodes were electrochemically prepared in a  $\text{Zn}/\text{MnO}_2$  cell with  $\beta\text{-MnO}_2$  as active materials ( $\text{MnO}_2\text{:CB:PVDF} = 7\text{:}2\text{:}1$ ) and 2 M  $\text{ZnSO}_4$  + 0.1 M  $\text{MnSO}_4$  as the electrolyte. The cells were pre-activated for 5 cycles between 0.8 and 1.8 V at  $0.1 \text{ A g}^{-1}$  and then discharged to 0.8 V at the end.

### 3. Results

#### 3.1. Characterization of the Prepared Materials

The PDI-EDA/EG composites were synthesized by a solution-based polymerization method, as illustrated in Figure 1a. Typically, EG, condensing agent EDA, and PTCDA monomers were first homogeneously dispersed into DMF. After solvothermal reaction, the PDI-EDA polymer was in situ polymerized on graphene nanosheets through  $\pi$ - $\pi$  stacking interactions. To optimize the ratio of EG to PDI-EDA, the mass ratios of EG to the composites were controlled to 1:9, 2:8, and 3:7 and named PDI-EDA/EG-10, PDI-EDA/EG-20, and PDI-EDA/EG-30, respectively. For comparison, pure PDI-EDA polymer was prepared under the same conditions in the absence of EG. The crystal structures of EG, PDI-EDA, and PDI-EDA/EG-20 were characterized by X-ray diffraction (XRD) and displayed in Figure 1b. XRD patterns of PDI-EDA show dominant peaks located at 11.8, 12.7, 25.3, 27.8, and 29.0°, which are attributed to the (011), (021), (112), (122), and (140) crystal planes of PDI-EDA, respectively [9,33,34]. In contrast, EG only demonstrates one broad peak at 26.7°. For the PDI-EDA/EG-20 composite, the five characteristic 2 $\theta$  peaks are still present, which indicates the presence of PDI-EDA in the composites. Importantly, the slightly lower intensity of the (021) peak in PDI-EDA/EG-20 than that of PDI-EDA indicated that the  $\pi$ - $\pi$  stacking interactions can reduce the degree of crystallinity of PDI-EDA, which is favorable for enhancing the electrochemical performance of organic electrodes due to the strengthened interactions between PDI-EDA and EG [9]. Fourier transform infrared spectra (FTIR) were performed to confirm the successful synthesis of these organic materials. As shown in Figure 1c, the adsorption peaks of PTCDA positioned at 1775.4, 1590.8, 1296.5, and 1014.6 cm<sup>-1</sup> are attributed to C = O bands bending vibration in carbonyl groups, C = C bands stretching vibration in benzenoid rings, and C-O-C and CO-O-CO bands stretching vibration in anhydrides, respectively [9,34,39]. In the spectrum of PDI-EDA, all the anhydride bands have almost disappeared, while the new peak at 1358.9 cm<sup>-1</sup> is ascribed to the C-N stretching, manifesting the generation of imide groups [9,40]. The double adsorption peaks formed at 1694.1 and 1659.6 cm<sup>-1</sup> are assigned to the symmetric and asymmetric stretching vibrations of the carbonyl group in PDI-EDA, respectively [9,41]. Moreover, the FTIR spectrum of PDI-EDA/EG-20 shows similar adsorption peaks to PDI-EDA, demonstrating the existence of PDI-EDA. As shown in Figure 1d, Raman spectra were characterized to further investigate PDI-EDA and EG interactions in the composites. For PDI-EDA, the three peaks located at 1297.6, 1377.7, and 1580.2 cm<sup>-1</sup> are attributed to the stretching of the C-C bond, the bending of the C-H bond, and the stretching of the C = C bond in perylene, respectively [9,40]. The PDI-EDA/EG composite also displays three major peaks of PDI-EDA with a slight blue shift, verifying that the PDI-EDA was successfully polymerized on EG with enhanced  $\pi$ - $\pi$  stacking interactions, in good agreement with the XRD and FTIR results.

Scanning electron microscopy (SEM) was used to characterize the morphology of the obtained samples. As displayed in Figures 1e-h and S1, the pure PDI-EDA exhibited a tubular structure with a rough surface. In contrast, for the PDI-EDA/EG samples, the tubular structure disappeared and a nanosheet structure was presented, especially at high mass ratios of EG, revealing that the EG can suppress the overgrowth of the PDI-EDA polymer and form a sandwich structure. The measured average thickness of the EG and PDI-EDA/EG-10, PDI-EDA/EG-20, and PDI-EDA/EG-30 samples is 1.52, 43.8, 36.3, and 32.2 nm (Supplementary Figure S2), respectively. This unique structure can not only strengthen the interactions between EG and PDI-EDA but also accelerate the ion/electron transfer kinetics, thus delivering remarkable rate capability and a long life span.

#### 3.2. Electrochemical Performance of the Prepared Materials

Based on the above discussion, the PDI-EDA/EG samples are expected to deliver superior Zn<sup>2+</sup>-storage properties. The electrochemical performance of pure PDI-EDA and PDI-EDA/EG samples was evaluated in coin-type ZIBs with 2 M ZnSO<sub>4</sub> as electrolyte and Zn foil as counter and reference electrode. First, the working potential of

PDI-EDA/EG was optimized. As shown in Supplementary Figure S3, 0.15–1.2 V is preferable due to the limited HER. Figure 2a displays the initial three cyclic voltammetry (CV) profiles of the PDI-EDA/EG-20 electrode at a sweep rate of  $0.2 \text{ mV s}^{-1}$ . Obviously, all three CV curves exhibit similar cathodic and anodic peaks, demonstrating the high reversibility of the electrode. The first circuit is slightly dissimilar to the second and third circuits, which could be attributed to the irreversible reactions and the formation of a solid electrolyte interface (SEI) on the Zn anode surface [9,14]. The CV profiles of PDI-EDA, PDI-EDA/EG-10, and PDI-EDA/EG-30 electrodes are also collected for comparison (Supplementary Figure S4a,c,e). The galvanostatic charge/discharge (GCD) profiles of the four anodes at different current densities were recorded to compare their electrochemical performance (Figure 2b, Supplementary Figure S4b,d,f). Evidently, as the current densities increase, the PDI-EDA/EG samples show less capacity decay than the pure PDI-EDA, demonstrating their lower electrode polarization at high current densities.

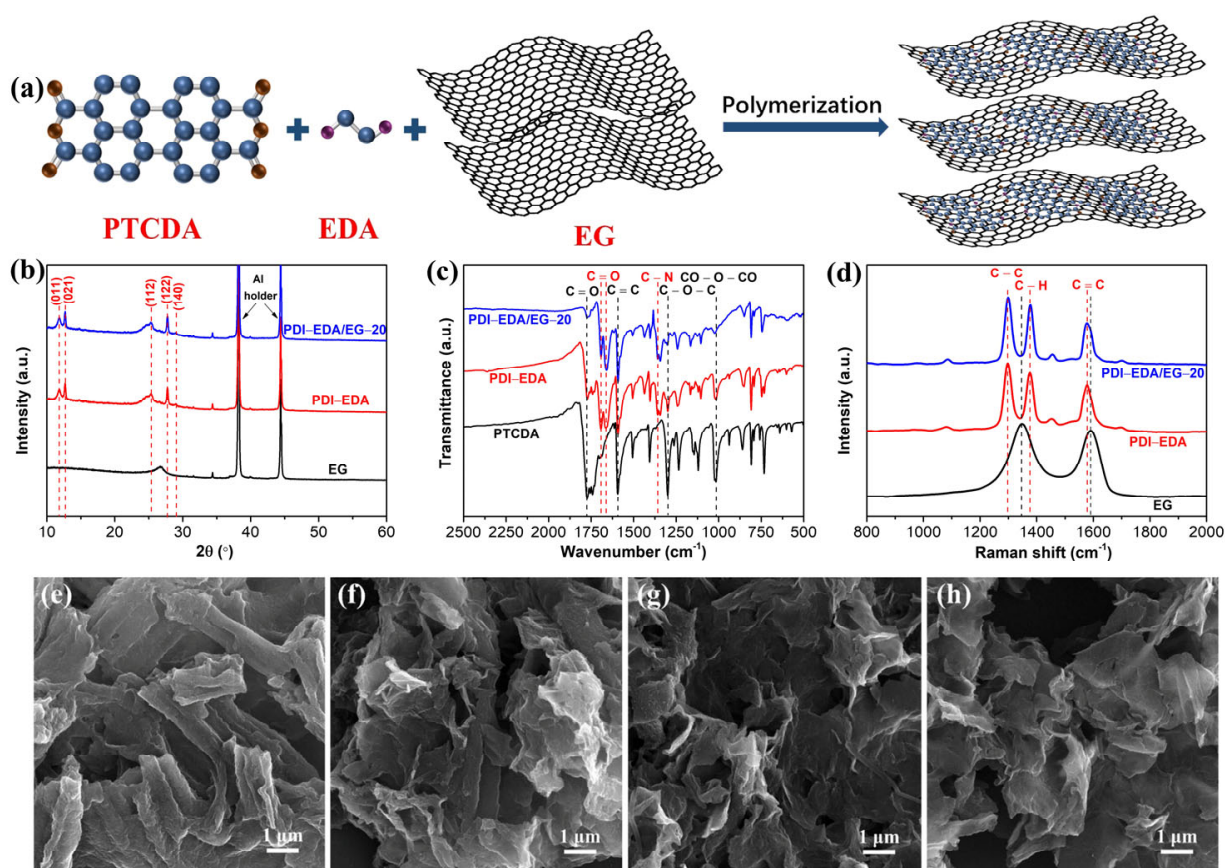


**Figure 1.** (a) Schematic of PDI-EDA/EG composite preparation. (b) XRD patterns, (c) FTIR spectra, and (d) Raman spectra of EG, PDI-EDA, PDI-EDA/EG-20. (e–h) SEM images of PDI-EDA, PDI-EDA/EG-10, PDI-EDA/EG-20, and PDI-EDA/EG-30 samples, respectively.

Based on the GCD profiles, the rate performance of the PDI-EDA, PDI-EDA/EG-10, PDI-EDA/EG-20, and PDI-EDA/EG-30 samples at various current densities is summarized in Figure 2c. For the pure PDI-EDA electrode, a discharge capacity of  $93.6 \text{ mAh g}^{-1}$  was delivered at  $0.1 \text{ A g}^{-1}$ , which decreased drastically to  $29.2 \text{ mAh g}^{-1}$  when the current density was increased to  $5 \text{ A g}^{-1}$ . In contrast, the PDI-EDA/EG electrodes possess improved rate capability. Especially for the PDI-EDA/EG-20 sample, a maximum capacity of  $110.2 \text{ mAh g}^{-1}$  can be obtained at a low current of  $0.1 \text{ A g}^{-1}$ , which can still maintain a capacity of  $88.9 \text{ mAh g}^{-1}$  at a high current density of  $5 \text{ A g}^{-1}$ . The superior rate performance should be attributed to the addition of EG, which can promote  $\text{Zn}^{2+}$  diffusion kinetics and facilitate charge transport. This result was further proven by electrochemical

impedance spectroscopy (EIS). As displayed in Figure 2d, the Nyquist plots of PDI-EDA and PDI-EDA/EG-20 exhibit a semicircle in the high frequency region and a straight line in the low frequency part, which represent the charge-transfer ( $R_{ct}$ ) resistance and  $Zn^{2+}$  diffusion resistance ( $R_D$ ), respectively. The intercept on the  $x$ -axis is associated with the bulk resistance ( $R_b$ ). Obviously, the PDI-EDA/EG-20 electrode demonstrates a higher slope, a smaller semicircle diameter, and an intercept, indicating accelerated ion/electron transfer in the presence of EG, explaining the better rate capability of PDI-EDA/EG-20 than PDI-EDA. The zinc-ion diffusion coefficient ( $D_{Zn^{2+}}$ ) can be analyzed by Equation (1) [42]:

$$D = R^2 T^2 / 2 A^2 n^4 F^4 C^2 \sigma^2 \quad (1)$$

where  $R$ ,  $T$ ,  $A$ ,  $n$ ,  $F$ ,  $C$ , and  $\sigma$  represent the gas constant, absolute temperature, electrode surface area, number of electrons per molecule oxidized, the Faraday constant, Zn ion concentration, and Warburg factor, respectively. The  $\sigma$  depends on  $Z'$ . As depicted in Supplementary Figure S5, evidently, the PDI-EDA/EG-20 electrode has a smaller slope value than the PDI-EDA electrode. The fast zinc-ion transport rate could be attributed to the hybrid sandwich nanosheet structure of the PDI-EDA/EG-20 anode, which facilitates electrolyte infiltration and electron migration. To evaluate the cycling performance of PDI-EDA and PDI-EDA/EG-20 anodes, the long-term cyclic stability at  $1 \text{ A g}^{-1}$  was tested. As shown in Figure 2e, the PDI-EDA/EG-20 electrode can maintain a capacity of  $82.9 \text{ mAh g}^{-1}$  with a capacity retention of 93.4% and nearly 100% coulombic efficiency after 1000 cycles, much higher than those of the bare PDI-EDA electrode ( $54.9 \text{ mAh g}^{-1}$  and 81.7% capacity retention).

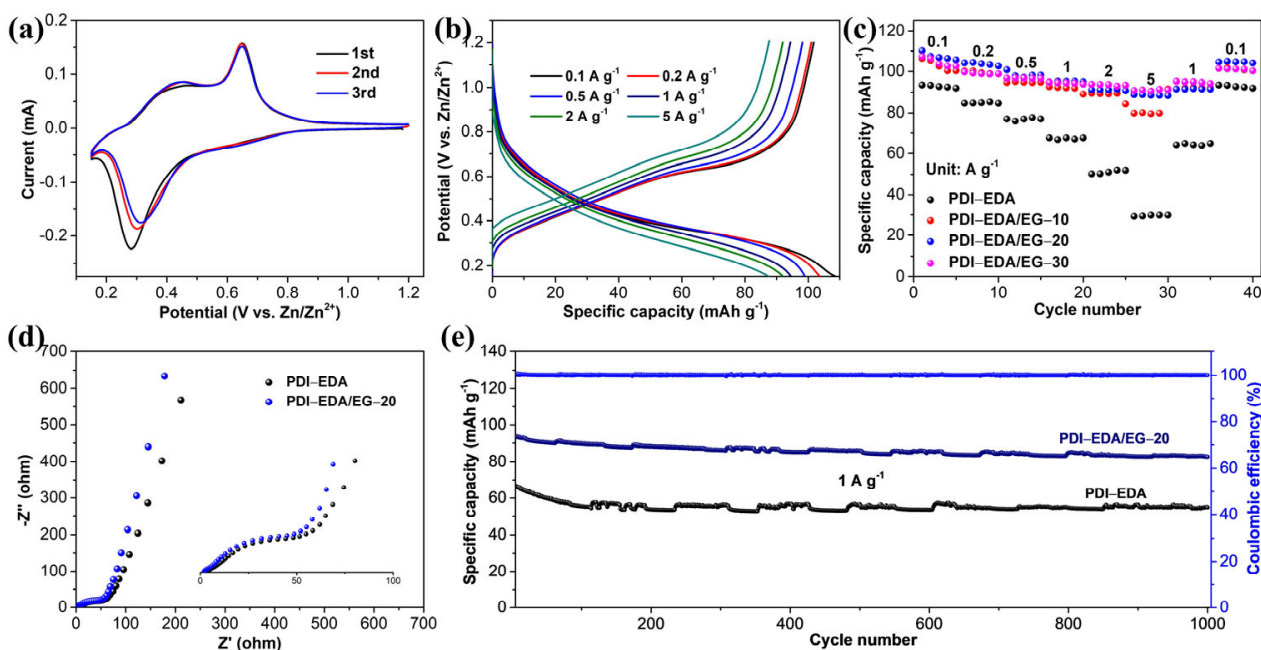


**Figure 2.** (a) Initial three CV curves of the PDI-EDA/EG-20 electrode at a sweep rate of  $0.2 \text{ mV s}^{-1}$ . (b) GCD profiles of the PDI-EDA/EG-20 electrode at various current densities. (c) Nyquist plots of PDI-EDA and PDI-EDA/EG-20 electrodes. (d) Rate performance of different anodes. (e) Long-term cycle stability test at  $1 \text{ A g}^{-1}$  for PDI-EDA and PDI-EDA/EG-20 anodes.

### 3.3. $Zn^{2+}$ Storage Mechanism in PDI-EDA/EG Materials

To examine the fast electrochemical reaction kinetics of  $Zn^{2+}$  storage in the PDI-EDA/EG-20 electrode, the CV profiles at different sweep rates were conducted ( $0.2$ – $2 \text{ mV s}^{-1}$ ) and shown in Figure 3a. All the CV curves exhibit similar shapes without obvious peak deviations as the sweep rate increases, manifesting highly reversible redox reactions. The relationship between the obtained peak current ( $i$ ) and sweep rate ( $v$ ) can be

used to quantitatively evaluate the  $\text{Zn}^{2+}$  storage kinetics by the power-law formula [25,42]:  $i = av^b$ , where  $b = 0.5$  suggests a diffusion-controlled process, while  $b = 1.0$  indicates a pseudocapacitive behavior [9,42]. As for the PDI-EDA/EG-20 electrode, the  $b$  values of 1, 2, and 3 peaks can be calculated to be 0.83, 0.97, and 0.86 (Figure 3b), respectively, demonstrating a fast pseudocapacitive process instead of solid-state diffusion for  $\text{Zn}^{2+}$ -storage. The  $b$  values of PDI-EDA (Supplementary Figure S6a,b), PDI-EDA/EG-10 (Supplementary Figure S6c,d), and PDI-EDA/EG-30 (Supplementary Figure S6e,f) electrodes are also calculated for comparison. In order to quantify the pseudocapacitive contribution ratio, the whole capacity can be divided into pseudocapacitive contribution ( $k_1v$ ) and diffusion-controlled contribution ( $k_2v^{1/2}$ ) under fixed potential ( $V$ ) by the equation:  $i(V) = k_1v + k_2v^{1/2}$  [42,43]. Figure 4c summarizes the proportions of pseudocapacitive contribution in PDI-EDA and PDI-EDA/EG-20 electrodes. The pseudocapacitive contribution ratios of the PDI-EDA/EG-20 electrode at 0.3, 0.5, 0.7, 1, and 2  $\text{mV s}^{-1}$  were 59.1, 74.1, 78.9, 85.1, and 93.9%, respectively, which were significantly higher than those of the PDI-EDA anode. This further verified that the presence of EG can improve the pseudocapacitive contribution of PDI-EDA/EG-20 with enhanced ionic/electronic conductivity, thus delivering remarkable rate capability and cycling stability. Furthermore, the galvanostatic intermittent titration technique (GITT) was performed to assess the detailed electrochemical reaction kinetics during GCD processes (Figures 3d and S7a). The corresponding  $\text{Zn}^{2+}$  diffusion coefficients ( $D_{\text{Zn}^{2+}}$ ) of PDI-EDA/EG-20 and PDI-EDA electrodes at different potentials could be calculated using the following equation [42]:

$$D = \frac{4L^2}{\pi\tau} \left( \frac{\Delta E_s}{\Delta E_t} \right)^2 \quad (2)$$

where  $L$ ,  $\tau$ ,  $\Delta E_s$ , and  $\Delta E_t$  are representing the thickness of the electrode (cm), the duration of the current pulse, the change in steady-state voltage, and the total change in cell voltage during the constant current pulse  $\tau$  after IR-drop in a single-step GITT experiment. As depicted in Figures 3e and S7b, the  $\text{Zn}^{2+}$  diffusion coefficients of the PDI-EDA/EG-20 anode are generally higher than those of pure PDI-EDA in the first and second discharge/charge processes, which is attributed to the enlarged surface area in PDI-EDA/EG-20 that ensures fast and vast  $\text{Zn}^{2+}$  storage. This analysis agrees with the EIS result and explains its exceptional rate capability and cycling stability.

In order to shed light on the  $\text{Zn}^{2+}$  storage behavior of the PDI-EDA/EG-20 anode, ex-situ FTIR and XPS were performed. As shown in Figure 4a, in the FTIR spectra of the as-prepared sample, the dual adsorption peaks located at 1694.1 and 1659.6  $\text{cm}^{-1}$  are assigned to the asymmetric and symmetric stretching vibrations of the C = O bond, respectively [9]. When the electrode is completely discharged, the adsorption peak at 1694.1  $\text{cm}^{-1}$  will be weakened. Meanwhile, two new peaks positioned at 1102.5 and 1022.4  $\text{cm}^{-1}$  appeared, which could be attributed to the stretching vibration of C-O and O-Zn bonds, manifesting the reduction of the C = O bond and the formation of the C-O-Zn bond [9,33]. When the electrode was completely charged, the adsorption peak at 1694.1  $\text{cm}^{-1}$  was restored, while the new peaks at 1102.5 and 1022.4  $\text{cm}^{-1}$  almost vanished, demonstrating that the redox reaction of the C = O bond and the uptake/release of  $\text{Zn}^{2+}$  are highly reversible [9]. In addition, the perylene ring and the C-N bond presented at 1588.6 and 1343.5  $\text{cm}^{-1}$  barely changed during the whole discharge/charge process, indicating that these functional groups were not involved in Zn storage [40,41].

To further elucidate the chemical bond evolution during discharge/charge, ex-situ XPS was employed (Supplementary Figure S8, Figure 4b–d). As demonstrated in the full XPS survey of the as-prepared electrodes (Supplementary Figure S8), the three clear peaks presented at 530.3, 399.2, and 281.6 eV are attributed to the O 1s, N 1s, and C 1s peaks, respectively [40]. As displayed in Figure 4b, in the high resolution Zn 2p spectra, two new peaks centered at 1044.7 and 1021.6 eV were formed after full discharge, indicating that  $\text{Zn}^{2+}$  is inserted into the PDI-EDA/EG-20 electrode. In the charge state, the peaks almost disappeared, suggesting that the electrochemical uptake/release of  $\text{Zn}^{2+}$  are highly

reversible. As displayed in the C 1s spectra of the as-prepared sample, the peaks positioned at 283.8, 284.8, and 289.8 eV could be associated with  $sp^2$  C = C,  $sp^3$  C-C, and C = O bonds, respectively [9]. After the electrode was completely discharged, the intensity of the C = C bond was weakened, while the C-C bond became stronger. Subsequently, the C = O bond disappeared, and a new peak at a lower binding energy of 288.6 eV was detected, which could be assigned to the reduction of the carbonyl group caused by  $Zn^{2+}$  coordination. On the other hand, after the electrode was recharged back to 1.2 V, the peaks almost recovered, indicating that the electrochemical reaction is highly reversible. This result was consistent with the high resolution of the O 1s spectra (Figure 4d), where the C = O/C-O bond intensity ratio decreased at the discharge state but increased after being fully charged. According to the above analyses, it can be concluded that the carbonyl group in PDI-EDA/EG-20 is the active site for the reversible uptake/release of  $Zn^{2+}$ .

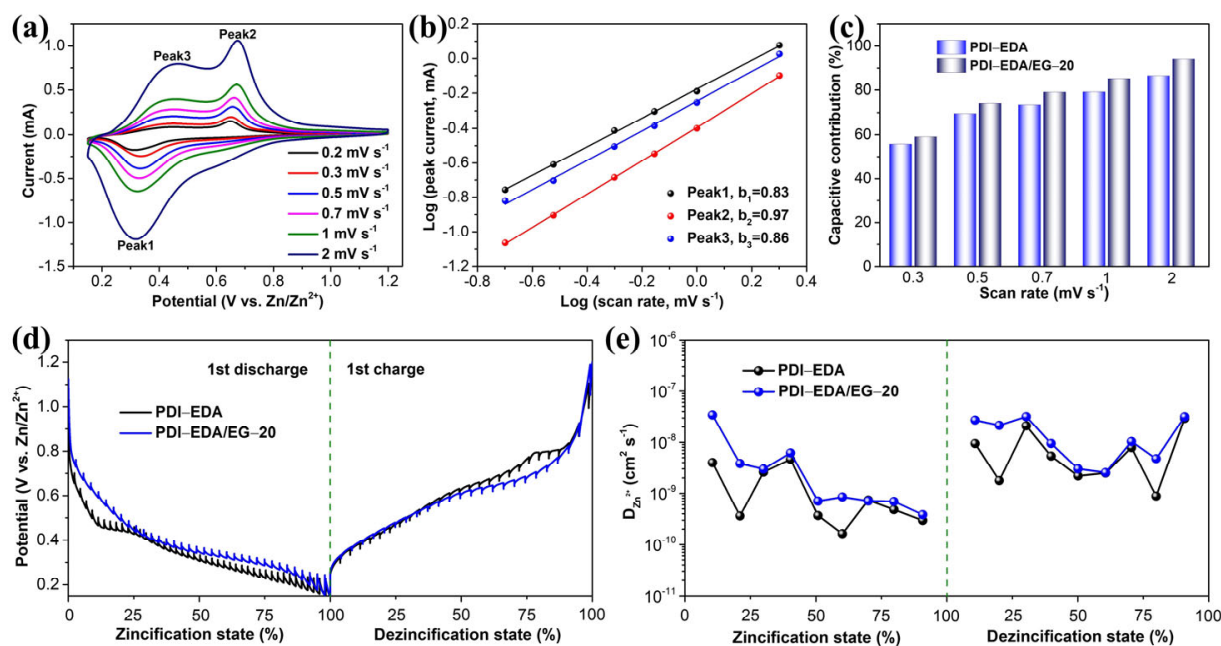


**Figure 3.** (a) CV profiles of the PDI-EDA/EG-20 electrode at different sweep rates. (b)  $b$  values for cathodic and anodic peaks of the PDI-EDA/EG-20 electrode. (c) Pseudocapacitive contribution of PDI-EDA and PDI-EDA/EG-20 at different sweep rates. (d) GITT curves and (e) corresponding  $Zn^{2+}$  diffusion coefficients at different potential states.

### 3.4. Assembly and Electrochemical Performance of a ZIB Full Cell

Finally, to explore the practical application of PDI-EDA/EG-20 in a ZIB full cell, a rocking-chair-type ZIB was constructed using a PDI-EDA/EG-20 anode and a pre-activated  $MnO_2$  cathode ( $Zn_xMnO_2$ ). The mass ratio of anode to cathode was adjusted to be 2:1. The electrochemical performance of the  $MnO_2$  cathode is shown in Supplementary Figure S9. Owing to the higher Zn storage potential than that of Zn plating and HER, employing PDI-EDA/EG-20 as an anode can effectively avoid electrolyte decomposition and dendrite formation, thereby boosting cycling stability. The schematic of the ZIB is demonstrated in Figure 5a. The typical CV profiles of the PDI-EDA/EG-20 anode,  $Zn_xMnO_2$  cathode, and PDI-EDA/EG-20// $Zn_xMnO_2$  full cell are depicted in Figure 5b. The first three CV profiles of the full ZIB are shown in Figure 5c. Obviously, all the CV profiles are almost overlapped, demonstrating the good electrochemical reversibility of the device. The CV profiles at sweep rates ranging from 0.5 to 5  $mV^{-1}$  were examined and are displayed in Figure 5d. All the curves demonstrate multiple reversible redox peaks without obvious deformation, manifesting the excellent electrochemical reversibility and fast kinetics of the cell. According to the power-law formula mentioned above, the  $b$  values of 1, 2, 3, and 4 peaks for the full ZIB can be calculated to be 0.86, 0.83, 0.80, and 0.99

(Supplementary Figure S10), respectively, indicating that the ZIB device undergoes a pseudocapacitive behavior, which is expected to display a superior rate capability. The GCD tests of the PDI-EDA/EG-20//Zn<sub>x</sub>MnO<sub>2</sub> battery were conducted and are shown in Figure 5e, where the current densities and capacities are calculated based on the anode and cathode active materials. At a low current density of 0.05 A g<sup>-1</sup>, the PDI-EDA/EG-20-based ZIB battery can deliver a high specific capacity of 64.6 mAh g<sup>-1</sup> and an average discharge plateau of 0.82 V. The battery could deliver specific capacities of 61.5, 56.8, 51.7, and 44.9 mAh g<sup>-1</sup> at 0.1, 0.2, 0.5, and 1 A g<sup>-1</sup>, respectively (Figure 5f.). Even at a high current density of 2 A g<sup>-1</sup>, the PDI-EDA/EG-20//Zn<sub>x</sub>MnO<sub>2</sub> battery can still yield a capacity of 38.9 mAh g<sup>-1</sup>, corresponding to a 60.3% capacity retention at 0.05 A g<sup>-1</sup>, showing exceptional rate performance. Figure 5g displays the cycling stability and coulombic efficiency (CE) of the PDI-EDA/EG-20//Zn<sub>x</sub>MnO<sub>2</sub> cell at 2 A g<sup>-1</sup>. Impressively, the cell exhibits no apparent capacity degradation after 1000 cycles with nearly 100% CE. Based on the GCD profiles, the energy density and power density of the PDI-EDA/EG-20//Zn<sub>x</sub>MnO<sub>2</sub> cell is calculated and the Ragone plots are demonstrated in Figure 5h. Significantly, the maximum energy density of the device can reach 54.9 Wh kg<sup>-1</sup> at a power of 42.5 W kg<sup>-1</sup>. Even at a high power density of 1523.4 W kg<sup>-1</sup>, the energy density can still keep at 29.4 Wh kg<sup>-1</sup>, manifesting the superior rate performance of the device. These values surpassed most reported “rocking-chair” ZIBs, including Na<sub>0.14</sub>TiS<sub>2</sub>//ZnMn<sub>2</sub>O<sub>4</sub> (51 Wh kg<sup>-1</sup>, 24.3 W kg<sup>-1</sup>) [28], PTCDI/rGO//ZnPB (44 Wh kg<sup>-1</sup>, 45.6 W kg<sup>-1</sup>) [37], Zn<sub>2</sub>Mo<sub>6</sub>S<sub>8</sub>//ZnPB (47 Wh kg<sup>-1</sup>, 12.8 W kg<sup>-1</sup>) [44], TiS<sub>2</sub>//Zn<sub>3</sub>V<sub>4</sub>(PO<sub>4</sub>)<sub>6</sub> (48.8 Wh kg<sup>-1</sup>, 51.7 W kg<sup>-1</sup>) [45], MoO<sub>2</sub>@NC//Zn-NVPOF (45.1 Wh kg<sup>-1</sup>, 44.3 W kg<sup>-1</sup>) [25], and PI-1/CNT//Zn<sub>x</sub>MnO<sub>2</sub> (50.5 Wh kg<sup>-1</sup>, 45.5 W kg<sup>-1</sup>) [39]. These results clearly imply that this hybrid polymer anode is a competitive candidate for high-power and long lifespan ZIBs.

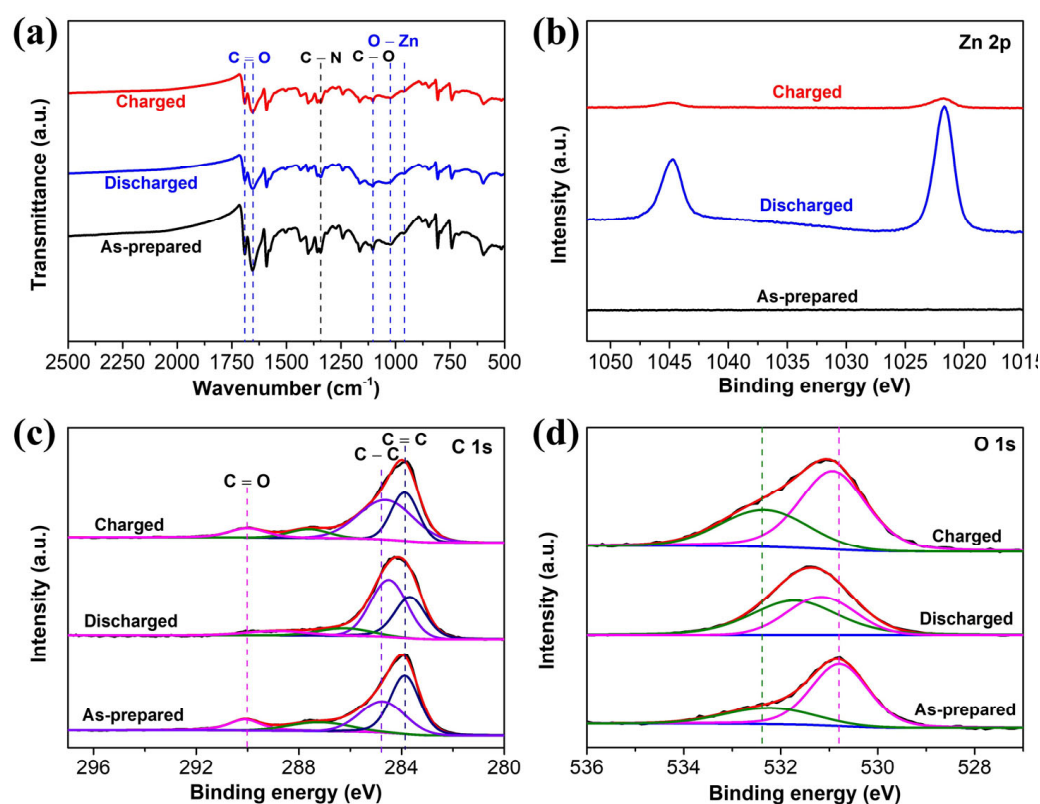


**Figure 4.** (a) FTIR spectra, (b) high-resolution Zn 2p spectra, (c) high-resolution C 1s spectra, and (d) O 1s spectra of PDI-EDA/EG-20 at different discharge/charge states.

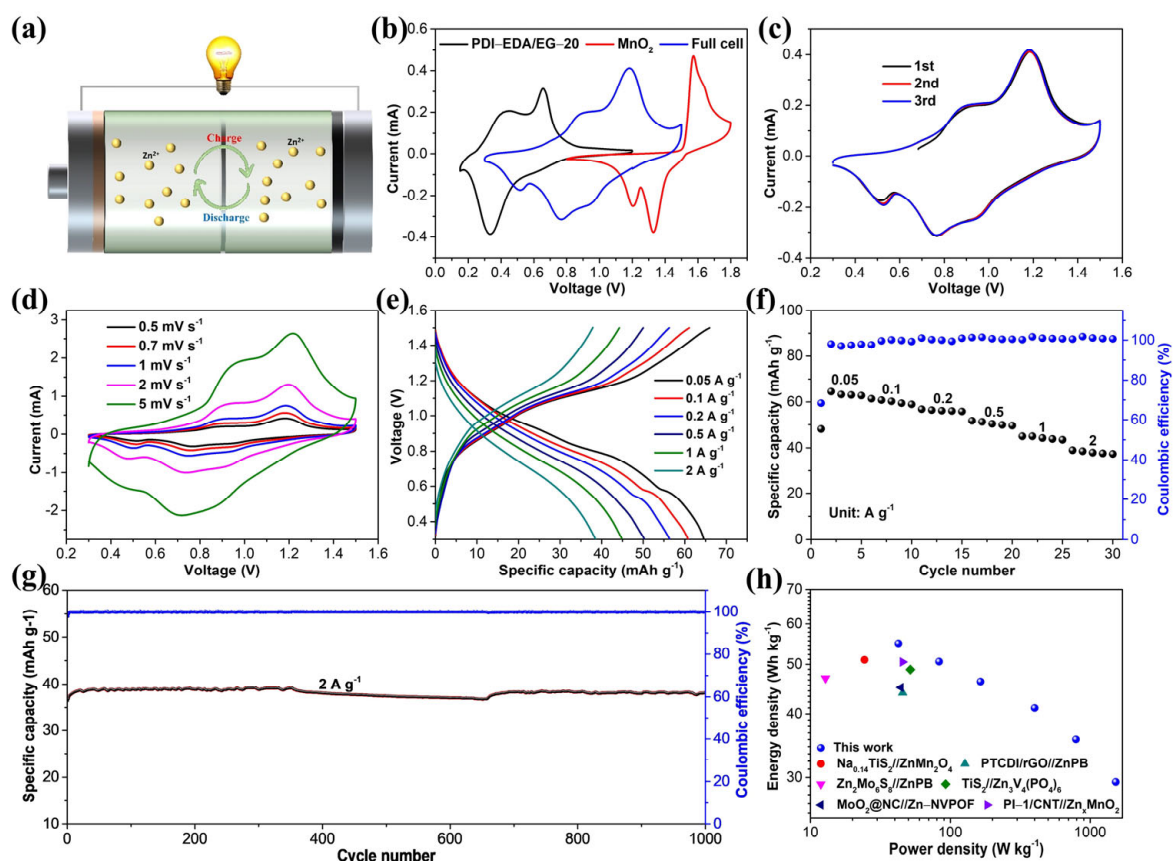


**Figure 5.** (a) Schematic of the fabricated ZIB device. (b) CV profiles of the PDI-EDA/EG-20 anode, the  $\text{MnO}_2$  cathode, and the ZIB full device. (c) Initial three CV profiles of the PDI-EDA/EG-20// $\text{Zn}_x\text{MnO}_2$  device. (d) CV profiles of the device at various sweep rates. (e) GCD profiles at different current densities. (f) Rate and (g) long-term cycling performance of the device. (h) Ragone plots of the ZIB in current work compared with previously reported ZIBs.

#### 4. Conclusions

In summary, a novel sandwich-structured PDI-EDA/EG hybrid material is designed and applied as an anode for aqueous “rocking-chair” ZIBs. The highly conductive graphene nanosheets and strong  $\pi$ - $\pi$  stacking interactions between graphene and PDI-EDA can accelerate the ion/electron migration and enhance the structural stability, thus delivering remarkable rate capability and cycling stability. When applied as an anode, it demonstrates a high capacity of  $110.2 \text{ mAh g}^{-1}$  at  $0.1 \text{ A g}^{-1}$  and keeps  $88.9 \text{ mAh g}^{-1}$  even at a high current density of  $5 \text{ A g}^{-1}$ . Various measurements, including ex-situ FTIR and ex-situ XPS, were performed to investigate the structure evolution during the discharge/charge process, revealing a reversible  $\text{Zn}^{2+}$  uptake/release at the carbonyl site of PDI-EDA/EG. More importantly, an aqueous “rocking-chair” ZIB was built by coupling a PDI-EDA/EG anode and  $\text{Zn}_x\text{MnO}_2$  cathode, which can realize an ultrahigh energy density of  $54.9 \text{ Wh kg}^{-1}$  and remarkable stability without capacity degradation after 1000 cycles at  $2 \text{ A g}^{-1}$ . This work offers an attractive anode material for aqueous ZIB, which may open a new avenue for the preparation of cost-effective and sustainable organic anodes for grid-scale applications.

**Supplementary Materials:** The following supporting information can be downloaded at: <https://www.mdpi.com/article/10.3390/batteries9060318/s1>, [46–55]. Figure S1: SEM images of (a,e) PDI-EDA, (b,f) PDI-EDA/EG-10, (c,g) PDI-EDA/EG-20, and (d,h) PDI-EDA/EG-30 composites, respectively; Figure S2: SEM images of (a) EG, (b) PDI-EDA/EG-10, (c) PDI-EDA/EG-20 and (d) PDI-EDA/EG-30 composites, respectively; Figure S3: CV curves of the PDI-EDA/EG-20 electrode at different potential windows; Figure S4: (a,c,e) CV curves and (b,d,f) GCD profiles of pure PDI-EDA, PDI-EDA/EG-10,

and PDI-EDA/EG-20 electrodes, respectively; Figure S5: The relationship between  $Z'$  and  $w^{-1/2}$  for the PDI-EDA and PDI-EDA/EG-20 electrodes; Figure S6: (a,c,e) CV curves at different current densities and (b,d,f)  $b$  values for anodic and cathodic peaks of PDI-EDA, PDI-EDA/EG-10, and PDI-EDA/EG-20 electrodes, respectively; Figure S7: (a) GITT curves and (b) corresponding  $Zn^{2+}$  diffusion coefficients at different potential states; Figure S8: Typical XPS survey of PDI-EDA/EG-20 electrode at different discharge/charge states; Figure S9: Electrochemical performance of  $MnO_2$  cathode. (a) Initial three CV curves. (b) CV curves at different sweep rates. (c) GCD profiles at different current densities. (d) Long-term cycling stability at  $2\text{ A g}^{-1}$ ; Figure S10: (a) CV curves of the device at different scan rates. (b)  $b$  values for cathodic and anodic peaks of the ZIB cell.

**Author Contributions:** Y.T. and S.L. contributed equally to this work. Data curation, Y.T.; writing—original draft preparation, S.L.; formal analysis, M.-F.L.; writing—review and editing, J.C. and A.L.-S.E.; supervision, Q.X. All authors have read and agreed to the published version of the manuscript.

**Funding:** This work was financially supported by the National Natural Science Foundation of China (Nos. 52102117, 51173170, and 21773216), the joint project from the Henan-Provincial and the China-National Natural Science Foundations (No. U2004208), and the Key Science and Technology Program of Henan Province (No. 202102310212).

**Institutional Review Board Statement:** Not applicable.

**Informed Consent Statement:** Not applicable.

**Data Availability Statement:** Not applicable.

**Acknowledgments:** The authors would like to thank Shiyanjia Lab ([www.shiyanjia.com](http://www.shiyanjia.com)) for assistance with SEM (28 December 2022), XRD (28 December 2022), Raman (28 December 2022), FTIR (5 January 2023), and XPS tests (5 January 2023).

**Conflicts of Interest:** The authors declare no conflict of interest.

## References

1. Li, H.; Firby, C.J.; Elezzabi, A.Y. Rechargeable Aqueous Hybrid  $Zn^{2+}/Al^{3+}$  Electrochromic Batteries. *Joule* **2019**, *3*, 2268–2278. [[CrossRef](#)]
2. Jia, X.; Liu, C.; Neale, Z.G.; Yang, J.; Cao, G. Active Materials for Aqueous Zinc Ion Batteries: Synthesis, Crystal Structure, Morphology, and Electrochemistry. *Chem. Rev.* **2020**, *120*, 7795–7866. [[CrossRef](#)]
3. Liu, H.; Wang, J.-G.; You, Z.; Wei, C.; Kang, F.; Wei, B. Rechargeable aqueous zinc-ion batteries: Mechanism, design strategies and future perspectives. *Mater. Today* **2021**, *42*, 73–98. [[CrossRef](#)]
4. Lv, Y.; Xiao, Y.; Ma, L.; Zhi, C.; Chen, S. Recent Advances in Electrolytes for “Beyond Aqueous” Zinc-Ion Batteries. *Adv. Mater.* **2022**, *34*, e2106409. [[CrossRef](#)] [[PubMed](#)]
5. Wang, D.; Li, Q.; Zhao, Y.; Hong, H.; Li, H.; Huang, Z.; Liang, G.; Yang, Q.; Zhi, C. Insight on Organic Molecules in Aqueous Zn-Ion Batteries with an Emphasis on the Zn Anode Regulation. *Adv. Energy Mater.* **2022**, *12*, 2102707. [[CrossRef](#)]
6. Liang, Y.; Cao, S.; Wei, Q.; Zeng, R.; Zhao, J.; Li, H.; Yu, W.W.; Zou, B. Reversible  $Zn^{2+}$  Insertion in Tungsten Ion-Activated Titanium Dioxide Nanocrystals for Electrochromic Windows. *Nano-Micro Lett.* **2021**, *13*, 196. [[CrossRef](#)]
7. Jiang, B.; Huang, T.; Yang, P.; Xi, X.; Su, Y.; Liu, R.; Wu, D. Solution-processed perylene diimide-ethylene diamine cathodes for aqueous zinc ion batteries. *J. Colloid Inter. Sci.* **2021**, *598*, 36–44. [[CrossRef](#)]
8. Zhang, L.; Chen, Y.; Jiang, Z.; Chen, J.; Wei, C.; Wu, W.; Li, S.; Xu, Q. Cation-Anion Redox Active Organic Complex for High Performance Aqueous Zinc Ion Battery. *Energy Environ. Mater.* **2022**, e12507. [[CrossRef](#)]
9. Cui, H.; Ma, L.; Huang, Z.; Chen, Z.; Zhi, C. Organic materials-based cathode for zinc ion battery. *SmartMat* **2022**, *3*, 565–581. [[CrossRef](#)]
10. Wang, Q.; Liu, Y.; Wang, C.; Xu, X.; Zhao, W.; Li, Y.; Dong, H. Vat Orange 7 as an organic electrode with ultrafast hydronium-ion storage and super-long life for rechargeable aqueous zinc batteries. *Chem. Eng. J.* **2023**, *451*, 138776. [[CrossRef](#)]
11. Li, H.; McRae, L.; Firby, C.J.; Elezzabi, A.Y. Rechargeable Aqueous Electrochromic Batteries Utilizing Ti-Substituted Tungsten Molybdenum Oxide Based  $Zn^{2+}$  Ion Intercalation Cathodes. *Adv. Mater.* **2019**, *31*, e1807065. [[CrossRef](#)] [[PubMed](#)]
12. Zhang, W.; Li, H.; Yu, W.W.; Elezzabi, A.Y. Transparent inorganic multicolour displays enabled by zinc-based electrochromic devices. *Light Sci. Appl.* **2020**, *9*, 121. [[CrossRef](#)] [[PubMed](#)]
13. Wang, W.; Kale, V.S.; Cao, Z.; Lei, Y.; Kandambeth, S.; Zou, G.; Zhu, Y.; Abouhamad, E.; Shekhah, O.; Cavallo, L.; et al. Molecular Engineering of Covalent Organic Framework Cathodes for Enhanced Zinc-Ion Batteries. *Adv. Mater.* **2021**, *33*, e2103617. [[CrossRef](#)]
14. Wang, X.; Liu, Y.; Wei, Z.; Hong, J.; Liang, H.; Song, M.; Zhou, Y.; Huang, X. MXene-Boosted Imine Cathodes with Extended Conjugated Structure for Aqueous Zinc-Ion Batteries. *Adv. Mater.* **2022**, *34*, e2206812. [[CrossRef](#)] [[PubMed](#)]

15. Yang, J.; Yin, B.; Sun, Y.; Pan, H.; Sun, W.; Jia, B.; Zhang, S.; Ma, T. Zinc Anode for Mild Aqueous Zinc-Ion Batteries: Challenges, Strategies, and Perspectives. *Nano-Micro Lett.* **2022**, *14*, 42. [[CrossRef](#)] [[PubMed](#)]
16. Xie, D.; Sang, Y.; Wang, D.H.; Diao, W.Y.; Tao, F.Y.; Liu, C.; Wang, J.W.; Sun, H.Z.; Zhang, J.P.; Wu, X.L. ZnF<sub>2</sub>-Richted Inorganic/Organic Hybrid SEI: In situ-Chemical Construction and Performance-Improving Mechanism for Aqueous Zinc-ion Batteries. *Angew. Chem. Int. Ed. Engl.* **2023**, *62*, e202216934. [[CrossRef](#)]
17. Li, C.; Xie, X.; Liang, S.; Zhou, J. Issues and Future Perspective on Zinc Metal Anode for Rechargeable Aqueous Zinc-ion Batteries. *Energy Environ. Mater.* **2020**, *3*, 146–159. [[CrossRef](#)]
18. Zhang, N.; Huang, S.; Yuan, Z.; Zhu, J.; Zhao, Z.; Niu, Z. Direct Self-Assembly of MXene on Zn Anodes for Dendrite-Free Aqueous Zinc-Ion Batteries. *Angew. Chem. Int. Ed. Engl.* **2021**, *60*, 2861–2865. [[CrossRef](#)]
19. Huang, S.; Hou, L.; Li, T.; Jiao, Y.; Wu, P. Antifreezing Hydrogel Electrolyte with Ternary Hydrogen Bonding for High-Performance Zinc-Ion batteries. *Adv. Mater.* **2022**, *34*, 2110140. [[CrossRef](#)]
20. Wu, M.; Zhang, Y.; Xu, L.; Yang, C.; Hong, M.; Cui, M.; Clifford, B.C.; He, S.; Jing, S.; Yao, Y.; et al. A sustainable chitosan-zinc electrolyte for high-rate zinc-metal batteries. *Matter* **2022**, *5*, 3402–3416. [[CrossRef](#)]
21. Xu, L.; Meng, T.; Zheng, X.; Li, T.; Brozena, A.H.; Mao, Y.; Zhang, Q.; Clifford, B.C.; Rao, J.; Hu, L. Nanocellulose-Carboxymethylcellulose Electrolyte for Stable, High-Rate Zinc-Ion Batteries. *Adv. Funct. Mater.* **2023**, 2302098. [[CrossRef](#)]
22. Wang, B.; Yan, J.; Zhang, Y.; Ye, M.; Yang, Y.; Li, C.C. In Situ Carbon Insertion in Laminated Molybdenum Dioxide by Interlayer Engineering Toward Ultrastable “Rocking-Chair” Zinc-Ion Batteries. *Adv. Funct. Mater.* **2021**, *31*, 2102827. [[CrossRef](#)]
23. Wang, X.; Wang, Y.; Jiang, Y.; Li, X.; Liu, Y.; Xiao, H.; Ma, Y.; Huang, Y.Y.; Yuan, G. Tailoring Ultrahigh Energy Density and Stable Dendrite-Free Flexible Anode with Ti<sub>3</sub>C<sub>2</sub>T<sub>x</sub> MXene Nanosheets and Hydrated Ammonium Vanadate Nanobelts for Aqueous Rocking-Chair Zinc-Ion Batteries. *Adv. Funct. Mater.* **2021**, *31*, 2103210. [[CrossRef](#)]
24. Liu, Y.; Huang, M.; Xiong, F.; Zhu, J.; An, Q. Improved zinc-ion storage performance of the metal-free organic anode by the effect of binder. *Chem. Eng. J.* **2022**, *428*, 131092. [[CrossRef](#)]
25. Li, W.; Ma, Y.; Shi, H.; Jiang, K.; Wang, D. Cu<sub>7</sub>Te<sub>4</sub> as an Anode Material and Zn Dendrite Inhibitor for Aqueous Zn-Ion Battery. *Adv. Funct. Mater.* **2022**, *32*, 2205602. [[CrossRef](#)]
26. Cheng, Y.; Luo, L.; Zhong, L.; Chen, J.; Li, B.; Wang, W.; Mao, S.X.; Wang, C.; Sprenkle, V.L.; Li, G.; et al. Highly Reversible Zinc-Ion Intercalation into Chevrel Phase Mo<sub>6</sub>S<sub>8</sub> Nanocubes and Applications for Advanced Zinc-Ion Batteries. *ACS Appl. Mater. Inter.* **2016**, *8*, 13673–13677. [[CrossRef](#)] [[PubMed](#)]
27. Kaveevivitchai, W.; Manthiram, A. High-capacity zinc-ion storage in an open-tunnel oxide for aqueous and nonaqueous Zn-ion batteries. *J. Mater. Chem. A* **2016**, *4*, 18737–18741. [[CrossRef](#)]
28. Li, W.; Wang, K.; Cheng, S.; Jiang, K. An Ultrastable Presodiated Titanium Disulfide Anode for Aqueous “Rocking-Chair” Zinc Ion Battery. *Adv. Energy Mater.* **2019**, *9*, 1900993. [[CrossRef](#)]
29. Cao, J.; Zhang, D.; Yue, Y.; Wang, X.; Srikrishna, A.; Sriprachabwong, C.; Tuantranont, A.; Zhang, X.; Wu, Z.-S.; Qin, J. Strongly coupled tungsten oxide/carbide heterogeneous hybrid for ultrastable aqueous rocking-chair zinc-ion batteries. *Chem. Eng. J.* **2021**, *426*, 131893. [[CrossRef](#)]
30. Lv, Z.; Wang, B.; Ye, M.; Zhang, Y.; Yang, Y.; Li, C.C. Activating the Stepwise Intercalation-Conversion Reaction of Layered Copper Sulfide toward Extremely High Capacity Zinc-Metal-Free Anodes for Rocking-Chair Zinc-Ion Batteries. *ACS Appl. Mater. Inter.* **2022**, *14*, 1126–1137. [[CrossRef](#)]
31. Lei, Q.; Zhang, J.; Liang, Z.; Yue, Y.; Ren, Z.; Sun, Y.; Yao, Z.; Li, J.; Zhao, Y.; Yin, Y.; et al. Synergistic Engineering of Sulfur Vacancies and Heterointerfaces in Copper Sulfide Anodes for Aqueous Zn-Ion Batteries with Fast Diffusion Kinetics and an Ultralong Lifespan. *Adv. Energy Mater.* **2022**, *12*, 2200547. [[CrossRef](#)]
32. Tian, G.; Wang, Q.; Qu, Z.; Yu, H.; Zhang, D.; Wang, Q. Coupling Engineering of NH<sup>4+</sup> Pre-Intercalation and Rich Oxygen Vacancies in Tunnel WO<sub>3</sub> Toward Fast and Stable Rocking Chair Zinc-Ion Battery. *Small* **2023**, *19*, e2206701. [[CrossRef](#)] [[PubMed](#)]
33. Huang, Y.; Li, K.; Liu, J.; Zhong, X.; Duan, X.; Shakir, I.; Xu, Y. Three-dimensional graphene/polyimide composite-derived flexible high-performance organic cathode for rechargeable lithium and sodium batteries. *J. Mater. Chem. A* **2017**, *5*, 2710–2716. [[CrossRef](#)]
34. Li, J.; Luo, M.; Ba, Z.; Wang, Z.; Chen, L.; Li, Y.; Li, M.; Li, H.-B.; Dong, J.; Zhao, X.; et al. Hierarchical multicarbonyl polyimide architectures as promising anode active materials for high-performance lithium/sodium ion batteries. *J. Mater. Chem. A* **2019**, *7*, 19112–19119. [[CrossRef](#)]
35. Yu, F.; Wang, Y.; Liu, Y.; Hui, H.-Y.; Wang, F.-X.; Li, J.-F.; Wang, Q. An aqueous rechargeable zinc-ion battery on basis of an organic pigment. *Rare Met.* **2022**, *41*, 2230–2236. [[CrossRef](#)]
36. Zhang, H.; Fang, Y.; Yang, F.; Liu, X.; Lu, X. Aromatic organic molecular crystal with enhanced  $\pi$ - $\pi$  stacking interaction for ultrafast Zn-ion storage. *Energy Environ. Sci.* **2020**, *13*, 2515–2523. [[CrossRef](#)]
37. Liu, N.; Wu, X.; Zhang, Y.; Yin, Y.; Sun, C.; Mao, Y.; Fan, L.; Zhang, N. Building High Rate Capability and Ultrastable Dendrite-Free Organic Anode for Rechargeable Aqueous Zinc Batteries. *Adv. Sci.* **2020**, *7*, 2000146. [[CrossRef](#)]
38. Parvez, K.; Wu, Z.-S.; Li, R.; Liu, X.; Graf, R.; Feng, X.; Muellen, K. Exfoliation of Graphite into Graphene in Aqueous Solutions of Inorganic Salts. *J. Am. Chem. Soc.* **2014**, *136*, 6083–6091. [[CrossRef](#)]
39. Xu, Z.; Li, M.; Sun, W.; Tang, T.; Lu, J.; Wang, X. An Ultrafast, Durable, and High-Loading Polymer Anode for Aqueous Zinc-Ion Batteries and Supercapacitors. *Adv. Mater.* **2022**, *34*, e2200077. [[CrossRef](#)]
40. Wu, D.; Zhang, G.; Lu, D.; Ma, L.; Xu, Z.; Xi, X.; Liu, R.; Liu, P.; Su, Y. Perylene diimide-diamine/carbon black composites as high performance lithium/sodium ion battery cathodes. *J. Mater. Chem. A* **2018**, *6*, 13613–13618. [[CrossRef](#)]

41. Li, S.; Tian, Q.; Chen, J.; Chen, Y.; Guo, P.; Wei, C.; Cui, P.; Jiang, J.; Li, X.; Xu, Q. An intrinsically non-flammable organic electrolyte for wide temperature range supercapacitors. *Chem. Eng. J.* **2023**, *457*, 141265. [[CrossRef](#)]
42. Li, S.; Chen, J.; Xiong, J.; Gong, X.; Ciou, J.; Lee, P.S. Encapsulation of MnS Nanocrystals into N, S-Co-doped Carbon as Anode Material for Full Cell Sodium-Ion Capacitors. *Nano-Micro Lett.* **2020**, *12*, 34.
43. Du, Y.; Zhang, B.; Kang, R.; Zhou, W.; Qin, J.; Wan, J.; Zhang, J.; Chen, G. Practical conversion-type titanium telluride anodes for high-capacity long-lifespan rechargeable aqueous zinc batteries. *J. Mater. Chem. A* **2022**, *10*, 16976–16985. [[CrossRef](#)]
44. Chae, M.S.; Hong, S.-T. Prototype System of Rocking-Chair Zn-Ion Battery Adopting Zinc Chevrel Phase Anode and Rhombohedral Zinc Hexacyanoferrate Cathode. *Batteries* **2019**, *5*, 3. [[CrossRef](#)]
45. Zhao, D.; Chen, S.; Lai, Y.; Ding, M.; Cao, Y.; Chen, Z. A stable “rocking-chair” zinc-ion battery boosted by low-strain  $Zn_3V_4(PO_4)_6$  cathode. *Nano Energy* **2022**, *100*, 107520. [[CrossRef](#)]
46. Luo, Y.; Zheng, F.; Liu, L.; Lei, K.; Hou, X.; Xu, G.; Meng, H.; Shi, J.; Li, F. A High-Power Aqueous Zinc-Organic Radical Battery with Tunable Operating Voltage Triggered by Selected Anions. *ChemSusChem* **2020**, *13*, 2239–2244. [[CrossRef](#)] [[PubMed](#)]
47. Glatz, H.; Lizundia, E.; Pacifico, F.; Kundu, D. An Organic Cathode Based Dual-Ion Aqueous Zinc Battery Enabled by a Cellulose Membrane. *ACS Appl. Energ. Mater.* **2019**, *2*, 1288–1294. [[CrossRef](#)]
48. Wan, F.; Zhang, L.; Wang, X.; Bi, S.; Niu, Z.; Chen, J. An Aqueous Rechargeable Zinc-Organic Battery with Hybrid Mechanism. *Adv. Funct. Mater.* **2018**, *28*, 1804975. [[CrossRef](#)]
49. Wu, M.; Su, W.; Wang, X.; Liu, Z.; Zhang, F.; Luo, Z.; Yang, A.; Yeleken, P.; Miao, Z.; Huang, Y. Long-Life Aqueous Zinc-Organic Batteries with a Trimethyl Phosphate Electrolyte and Organic Cathode. *ACS Sustain. Chem. Eng.* **2023**, *11*, 957–964. [[CrossRef](#)]
50. Zhao, Q.; Huang, W.; Luo, Z.; Liu, L.; Lu, Y.; Li, Y.; Li, L.; Hu, J.; Ma, H.; Chen, J. High-capacity aqueous zinc batteries using sustainable quinone electrodes. *Sci. Adv.* **2018**, *4*, eaao1761. [[CrossRef](#)] [[PubMed](#)]
51. Guo, Z.; Ma, Y.; Dong, X.; Huang, J.; Wang, Y.; Xia, Y. An Environmentally Friendly and Flexible Aqueous Zinc Battery Using an Organic Cathode. *Angew. Chem. Int. Ed.* **2018**, *130*, 11911–11915. [[CrossRef](#)]
52. Zhang, H.; Zhong, L.; Xie, J.; Yang, F.; Liu, X.; Lu, X. A COF-Like N-Rich Conjugated Microporous Polytriphenylamine Cathode with Pseudocapacitive Anion Storage Behavior for High-Energy Aqueous Zinc Dual-Ion Batteries. *Adv. Mater.* **2021**, *33*, 2101857. [[CrossRef](#)]
53. Zhao, Y.; Huang, Y.; Wu, F.; Chen, R.; Li, L. High-Performance Aqueous Zinc Batteries Based on Organic/Organic Cathodes Integrating Multiredox Centers. *Adv. Mater.* **2021**, *33*, 2106469. [[CrossRef](#)] [[PubMed](#)]
54. Wang, X.; Wang, G.; He, X. Anthraquinone porous polymers with different linking patterns for high performance Zinc-Organic battery. *J. Colloid Interf. Sci.* **2023**, *629*, 434–444. [[CrossRef](#)] [[PubMed](#)]
55. Tie, Z.; Zhang, Y.; Zhu, J.; Bi, S.; Niu, Z. An Air-Rechargeable Zn/Organic Battery with Proton Storage. *J. Am. Chem. Soc.* **2022**, *144*, 10301–10308. [[CrossRef](#)] [[PubMed](#)]

**Disclaimer/Publisher’s Note:** The statements, opinions and data contained in all publications are solely those of the individual author(s) and contributor(s) and not of MDPI and/or the editor(s). MDPI and/or the editor(s) disclaim responsibility for any injury to people or property resulting from any ideas, methods, instructions or products referred to in the content.